

Coherent control of an NV^- center with one adjacent ^{13}C

Burkhard Scharfenberger,^{1,*} William J. Munro,^{2,1} and Kae Nemoto¹

¹*National Institute of Informatics, 2-1-2 Hitotsubashi, Chiyoda-ku, Tokyo 101-8430, Japan*

²*NTT Basic Research Laboratories, NTT Corporation,
3-1 Morinosato Wakamiya, Atsugi, Kanagawa 243-0198, Japan*

(Dated: October 19, 2018)

We investigate the theoretically achievable fidelities when coherently controlling an effective three qubit system consisting of a negatively charged nitrogen vacancy (NV^-) center in diamond with an additional nearby carbon ^{13}C spin $I_C = 1/2$ via square radio and microwave frequency pulses in different magnetic field regimes. Such a system has potentially interesting applications in quantum information related tasks such as distributed quantum computation or quantum repeater schemes. We find that the best fidelities can be achieved in an intermediate magnetic field regime. However, with only square pulses it will be challenging to reach the fidelity threshold(s) predicted by current models of fault-tolerant quantum computing.

PACS numbers: 03.67.Lx, 03.67.-a, 76.30.Mi

I. INTRODUCTION

Impurity spins in solids have long been known for their potential to be used in quantum information processing devices [1–3]. Among these, the negatively charged vacancy centers (NV^-) in diamond has stood out for its exceptional properties. It is a well localized, stable and optically controllable spin in the 'vacuum' of a mostly spin-less carbon lattice [4]. Given these virtues, they have early been recognized as a good solid state qubit, showing long coherence times even at room temperature [5–8]. Moreover, NV^- centers have been employed in a host of applications beyond quantum information, ranging from use as single photon source [9–11], high-resolution sensor in electrometry [12], magnetometry [8, 13–19], decoherence microscopy [20–22], nano-scale NMR sensor [23–25] and thermometer [26].

A nitrogen vacancy center consists of a vacancy site in a diamond lattice adjacent to a substitutional nitrogen atom resulting in a defect of $C_{3,v}$ symmetry [27, 28]. In the negative charge state NV^- , the electronic wave function is a spin $S=1$ for both a ground state manifold (GSM) with orbital symmetry A_2 as well as an excited state manifold (ESM) of E-type orbital symmetry separated from the GSM by an optical 637nm (ZPL) transition. The NV^- center exhibits the useful properties of optical polarizability and spin dependent fluorescence, allowing initialization and readout of the electronic spin even at room temperature. These are possible due to the presence of energetically intermediate levels between the GSM and ESM, which allow spin non-conserving, non-radiative transitions which preferentially (but not completely) populate the $m_S = 0$ sub-level (for a detailed review see [4]).

Together with the electronic spin of the vacancy, hyperfine-coupled nitrogen and possibly carbon nuclear

spins found in the vicinity can form a quantum register of several qubits. In such a register, the nuclear spins with their excellent coherence times [29, 30] would serve as quantum memories accessed via the more directly controllable electronic spin of the vacancy. This system was proposed as node in a quantum repeater [31, 32] as well as for quantum information processing [33] and has been intensely studied by numerous experiments both at room and at low temperature ($\approx 4-8K$). The important milestones demonstrated are initialization and single-shot readout of electronic and nuclear spins in both temperature regimes [34–36], as well as, at low temperature, creation of entanglement between vacancy electron and nuclear spins [37], the polarization of single photons [38] and other (distant) NV centers [39]. Further important steps on the way to a scalable quantum computation architecture are a demonstration of room temperature quantum registers formed by long-range dipolar coupled NV^- centers [40] and entanglement swapping to nuclear spins [41]. Moreover, in quantum registers made up of a single NV^- and multiple proximate carbon nuclear spins, decoherence-protected operations were performed [42], and recently the first implementations of quantum error correction in diamond-based qubits was also demonstrated [43, 44].

While these experiments serve as beautiful proofs-of-principle and fidelities achieved are remarkable given the practical technical difficulties, they are not yet at thresholds required for scaleable, fault-tolerant quantum computation [45]. In particular, even with error correction a general computation will require many gate executions before the system is reset/corrected and this quickly degrades fidelity. From the perspective of architecture selection and design, it would be highly desirable to have a better theoretical understanding of the ultimate limits to the achievable fidelities, given the inherent properties of the NV^- system. Previous studies looking at a bare NV^- center in a pure carbon lattice have shown that in principle such a system might indeed allow operations with high enough accuracy for large-scale quan-

*Electronic address: burkhard@nii.ac.jp

tum computation even when using only simple control pulses [46], at least as long as exciting the vacancy spin out of the GSM is avoided. The hyperfine interaction strength in the ESM ($\sim 60\text{MHz}$) is relatively stronger than in the GSM ($\sim 3\text{MHz}$) [47, 48], and hence any excitation from the GSM could result in dephasing on the nitrogen nuclear spin. As quantum information requires not only gate operation but also readout and initialization, this difference in coupling strength adds significant constraints on the operational regimes of physical parameters and setups. By contrast, nearby, strongly coupled ^{13}C nuclear spins do not show this difference in hyperfine coupling strength, and it might thus be used to design a device immune to this source of dephasing.

This leads to the question investigated in the present work: whether high-fidelity control by simple means is still possible in an effective three-qubit system ($^{15}\text{NV}^- + ^{13}\text{C}$), where the carbon introduces interactions which potentially make high-fidelity control more difficult.

This paper is structured as follows: in section II we introduce the effective spin model we use and discuss the magnetic field regimes we investigate it in, which are low magnetic field (low-B) and intermediate magnetic field (med-B). Of these, we first look at the low-B case in section III, investigating single-pulse single qubit control and entanglement creation via concatenated pulses. In section IV we move on to the intermediate magnetic field regime, where multi-qubit operations can also be achieved with single driving pulses. Section V contains an analysis of times and fidelities for derived gates based on the results from the previous section and finally we give a concluding discussion in section VI.

II. EFFECTIVE SPIN MODEL

The system we study consists of effectively three qubits: the electronic spins of the vacancy defect (V) and two nuclear spins, one belonging to the, always present, nitrogen and the other to a nearby carbon ^{13}C . Throughout we will assume the nitrogen to be a ^{15}N isotope, and thus both nuclei in our system have spin $I = 1/2$, while the electronic spin state is a triplet $S = 1$. Since we do not consider excitations out of the $^3\text{A}_2$ GSM, the free time evolution of the system is well described by the Hamiltonian [49]:

$$\begin{aligned}
H_{\text{NVC}} &= H_{\text{V}} + H_{\text{N}} + H_{\text{C}} + H_{\text{VN}} + H_{\text{VC}} \\
H_{\text{V}} &= DS_z^2 + \frac{1}{2}E(S_x^2 - S_y^2) + \gamma_e BS_z \\
H_{\text{C/N}} &= \gamma_{\text{C/N}} BI_{\text{C/N},z} \\
H_{\text{VN}} &= \vec{S}\vec{A}\vec{I}_{\text{N}} \\
H_{\text{VC}} &= \vec{S}\vec{C}\vec{I}_{\text{C}} ,
\end{aligned} \tag{1}$$

where $\vec{S} = (S_x, S_y, S_z)^T$ is the vacancy and $\vec{I} = (I_x, I_y, I_z)^T$ the nuclear spin operator and we define the

magnetic moments $\gamma_e = g_e\mu_{\text{B}} = 28\text{MHz/mT}$ for the electronic spin as well as the nuclear spins of carbon $\gamma_{\text{C}} = g_{\text{C}}\mu_{\text{n}} = +10.6\text{kHz/mT}$ and nitrogen $\gamma_{\text{N}} = g_{\text{N}}\mu_{\text{n}} = -4.3\text{kHz/mT}$. D is a zero-field splitting of 2.88GHz (at low temperature) coming from the spin-spin interaction, B denotes the magnetic field which we assume to be parallel to the NV-axis, and E is the crystal strain which is very weak in the GSM ($0\dots 10\text{MHz}$) and could be canceled entirely by applying an appropriate electric field. Finally, \vec{A} and \vec{C} are the hyperfine tensors of nitrogen and carbon respectively.

For symmetry reasons \vec{A} is exactly axial, while \vec{C} is approximately so, even for nearest neighbor carbons where one might expect the contact term to give a significant non-axial contribution. As we consider the nitrogen to be an ^{15}N isotope ($I = 1/2$), we do not need to include a nuclear quadrupolar term in (1). Also, the direct dipolar interaction between the two nuclear spins is negligible.

The hyperfine interaction term for the nitrogen consists of parallel and exchange contribution and reads $\vec{S}\vec{A}\vec{I}_{\text{N}} = A_{\parallel}S_zI_{\text{N},z} + \frac{1}{2}A_{\perp}(S^+I_{\text{N}}^- + S^-I_{\text{N}}^+)$. While the carbon hyperfine-term looks the same in its principal axis system, there are additional terms after transforming into NV-adapted coordinates (with z along the NV's symmetry axis):

$$\begin{aligned}
\vec{S}\vec{C}\vec{I}_{\text{C}} &= C_{\parallel}(\theta) S_z I_{\text{C},z} + \frac{1}{2}C_{\perp}(\theta) (S^+ I_{\text{C}}^- + S^- I_{\text{C}}^+) \\
&+ \frac{1}{2}C_{\text{R}}(\theta) (S^+ I_{\text{C}}^+ + S^- I_{\text{C}}^-) \\
&+ C_{\Delta}(\theta) (S_z I_{\text{C},y} + S_y I_{\text{C},z}) ,
\end{aligned} \tag{2}$$

where the C_{Δ} -term contains z - and y -operators because we used an x -axis rotation in the coordinate transformation. The four coefficients depend on the angle θ between the NV axis and the carbon vacancy axis and are given by

$$\begin{aligned}
C_{\parallel}(\theta) &= C_{\parallel} \cos^2 \theta + C_{\perp} \sin^2 \theta \\
C_{\perp}(\theta) &= \frac{1}{2} (C_{\perp} (1 + \cos^2 \theta) + C_{\parallel} \sin^2 \theta) \\
C_{\text{R}}(\theta) &= \frac{1}{2} (C_{\perp} (1 - \cos^2 \theta) - C_{\parallel} \sin^2 \theta) \\
C_{\Delta}(\theta) &= (C_{\perp} - C_{\parallel}) \sin \theta \cos \theta .
\end{aligned} \tag{3}$$

The effect of the two additional terms C_{R} and C_{Δ} on energy levels and states in the magnetic field regime are minimal except that for the $m_S = 0$ states at low field, where C_{R} causes a splitting between even parity states ($|0, \uparrow, \uparrow\rangle_{\text{VCN}}$ and $|0, \downarrow, \downarrow\rangle_{\text{VCN}}$) while the odd parity states ($|0, \uparrow, \downarrow\rangle_{\text{VCN}}$ and $|0, \downarrow, \uparrow\rangle_{\text{VCN}}$) are split by the exchange term.

The value for $C_{\parallel}(\theta)$ can be observed directly in ODMR experiments as the hyperfine splitting between different carbon spin orientations. The other parameters are, however, harder to confirm. A rough estimate can be gained by setting the magnetic field to $B = B_x = 103\text{mT}$ and observing the splitting at the avoided crossing between the

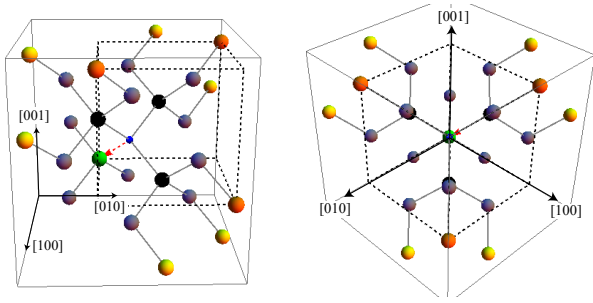


FIG. 1: **Carbon nuclear spin positions.** NV center and the sites where the lattice positions for the (one) carbon ^{13}C we considered in this study: on the left a free 3D view and on the right along the $[111]$ direction. The color coding of the spheres is as follows: (small) blue = vacancy, green = nitrogen, black = nearest neighbors (of V), gray = next nearest neighbors, yellow and orange: third neighbors for which numerical *ab-initio* calculations suggest strong hyperfine interaction with the vacancy spin due to finite spin density. These calculations find slightly different coupling strength for the two positions yellow and orange, but this has not yet been resolved experimentally. The dashed cage shows a diamond lattice unit-cell.

$m_S = -1$ and 0 levels. Since the Hamiltonian is highly connected, this will not yield good results even for C_{\perp} . A better strategy is measuring the level splitting while sweeping the magnetic field and fitting the model parameters to the obtained data. As an analytic approximation to this, one can look at the curvature of the $m_S = 0, -1$ levels in a field region around 60-80 mT. There, at least in 2nd-order perturbation theory, the curvatures are directly proportional to C_{\perp}^2 (mixing $|-1, \uparrow\rangle_{\text{VC}} \leftrightarrow |0, \downarrow\rangle_{\text{VC}}$) and $C_{\text{R}}^2 + C_{\Delta}^2$ respectively (mixing $|-1, \downarrow\rangle_{\text{VC}} \leftrightarrow |0, \uparrow\rangle_{\text{VC}}$).

We considered two different carbon positions, nearest neighbor and third-neighbor, because these show the strongest hyperfine interaction and thus offer the potentially fastest gate times. For a nearest neighbor carbon, hyperfine interaction strength in the principal basis is $C_{\parallel, \text{nn}} = 199\text{MHz}$ and $C_{\perp, \text{nn}} = 123\text{MHz}$ while in the NV-basis this corresponds to $C_{\parallel}(\theta_{\text{nn}}) = 129\text{MHz}$, $C_{\perp}(\theta_{\text{nn}}) = 155\text{MHz}$, $C_{\text{R}}(\theta_{\text{nn}}) = -35\text{MHz}$ and $C_{\Delta}(\theta_{\text{nn}}) = 25\text{MHz}$ ('nn' stands for 'nearest neighbor'). Numerical *ab-initio* calculations found two different classes of third-neighbor positions showing a strong hyperfine coupling [47]: planar (out of plane) third neighbors (see Figure 1) with coupling constants of $C_{\parallel, \text{3rd}} = 19$ (18) MHz and $C_{\perp, \text{3rd}} = 14$ (13) MHz. In ensemble measurements [50], hyperfine ESR lines associated w. third neighbors have been identified showing interaction strengths of $C_{\parallel}^{\text{3rd}} = 18.5$ and $C_{\perp}^{\text{3rd}} = 13.26$ which is right in between the theoretically predicted values. We use these latter values as the best estimate of third-neighbor interaction strength.

In comparison to the bare NV center, the level structure of the Hamiltonian (1) shows a much larger splitting of the $m_S = \pm 1$ levels due to the much stronger parallel hyperfine interaction for both carbon positions we considered. There are two avoided crossings, one strain-avoided

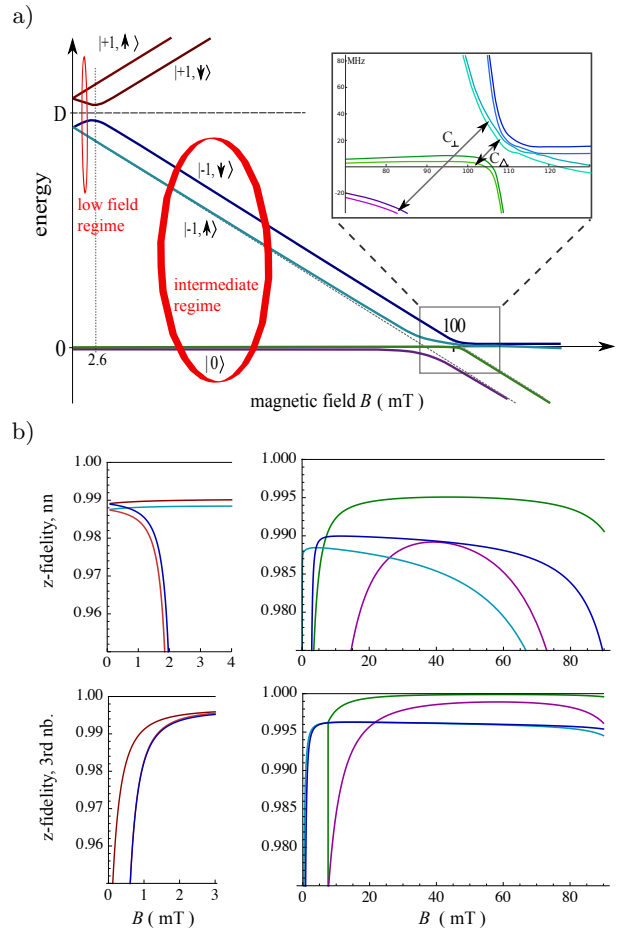


FIG. 2: **Levels and z-fidelity dependence on an axial magnetic field.** a.) Energy levels as function of magnetic field strength for nearest neighbor ^{13}C . The insets zoom in on the avoided crossings at $B = 2.6\text{mT}$ and 103mT respectively. For this plot, an unrealistically high strain was assumed in order to clearly show the former. b.) Fidelity of eigenstates with S_z, I_z -basis ('z-fidelity') for low- and intermediate magnetic field (left and right column respectively). Same colors represent the same states in both pictures.

at $B_{\text{str, nn}} = C_{\parallel}/2\gamma_e \approx 2.6\text{mT}$ ($B_{\text{str, 3rd}} = 0.28\text{mT}$ for third neighbors) and the other (mainly) exchange-avoided at $B_x = D/\gamma_e \approx 103\text{mT}$.

For the sake of simplicity in both analysis and application, it makes sense to investigate the model in magnetic field regimes where the eigenstates have high 'z-fidelity', *i.e.*, are close to the S_z, I_z -basis. In the NV $^-$, in principle three such regimes exist. The z-fidelity can be achieved for very high magnetic fields of $B \gg B_x$, for which the $|m_S = -1\rangle$ levels are lowest in energy. Such large magnetic fields are however not very desirable from a practical point of view, as they are difficult to keep stable and the fast Larmor precession of the electronic spin makes accurate timing harder. We therefore chose to concentrate on the low field and intermediate field strengths, which are around $B = 1 - 2\text{mT}$ and $B = 15 - 50\text{mT}$ respectively. For nearest neighbor ^{13}C , this is on either side

of the strain avoided crossing between $|+1\rangle_V$ and $|-1\rangle_V$ levels at $B = B_{\text{str, nn}}$ while for third neighbor carbons, both are above $B_{\text{str, 3rd}}$.

A. Decoherence Model

To simulate dissipative time evolution in our system, we solve a time-dependent master equation with Lindblad operators describing relaxation and dephasing for each subsystem individually (the details can be found in Appendix B) In order to model the experimentally well established gaussian dephasing of the vacancy spin [51, 52], we assumed time dependent rates $\gamma_{2,V,a/b}(t) = t/(T_{2,V}^*)^2$ (i.e. same for both dephasing channels a and b). Since the hyperfine coupling is quite strong for close-by carbons, one should in general use Lindblad operators adapted to the eigenbasis of the total system. However, since we are only interested in magnetic field regimes where the eigenbasis is very close to the computational (S_z - I_z) basis, the error due to the simplified decoherence model is inconsequential. The decoherence times we assumed were $T_{1,V} = 10\text{ms}$, $T_{2,V}^* = 100\mu\text{s}$, $T_{1,C} = T_{1,N} = 10\text{s}$, $T_{2,C} = T_{2,N} = 10\text{ms}$. These are conservative estimates, and each individually has already been demonstrated or even surpassed in experiment [6–8].

B. Driving

We model microwave (MW) and radio-frequency (RF) driving with a Hamiltonian of the form

$$H_{\text{drive}} = u(t) \left(S_x + \frac{\gamma_C}{\gamma_e} I_{C,x} + \frac{\gamma_N}{\gamma_e} I_{N,x} \right). \quad (4)$$

where the driving field is a sum square pulses $u(t) = \sum_{n=1}^{N_f} \Omega_{0,n} \cos(\nu_n t + \phi_0)$. The number of frequency components, N_f , was in practice either 1 or 2 and ν_n usually chosen in resonance with some transition. This leaves the $\Omega_{0,n}$ as the main parameter(s) to be optimized. However, we limited our search to values which are still in the RWA regime, so that the relative phase ϕ_0 provides control of the driving axis and a direct handle (direct coupling to y -direction operators) is unnecessary.

In this work we do not consider pulse shaping (varying Ω_0 and ϕ_0 continuously in time), leaving this as a further optimization to achieve fully fault-tolerant quantum computation in the future.

III. LOW FIELD

In this section, we present our results for the low magnetic field regime. As mentioned in the previous section, low magnetic fields offer the advantage of less stringent pulse timing requirements. Furthermore, in a scenario

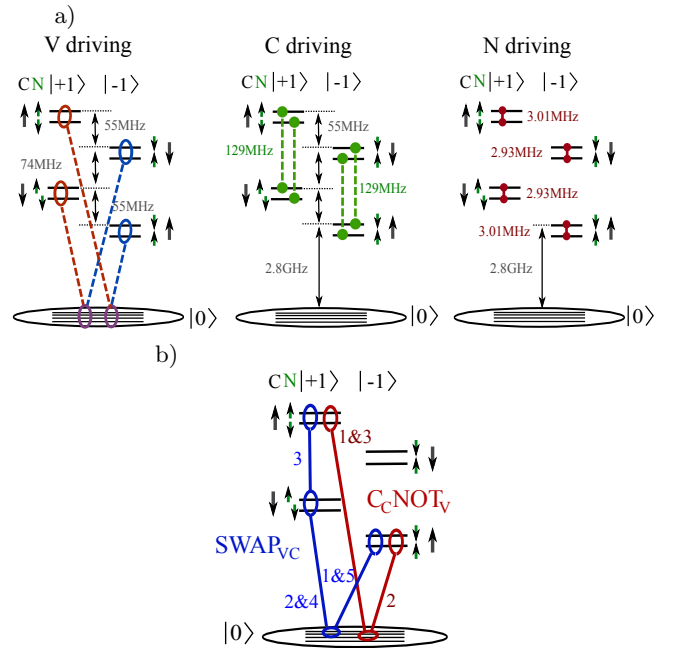


FIG. 3: **Transitions driven to obtain low B gates.** Level schematics and transition frequency values are for nearest neighbor carbon at $B = 1.1\text{mT}$. (a) Primitive transitions. Controlling the vacancy spin independent of the state of the carbon ^{13}C requires dual frequency pulses. (b) Two-qubit gates in the subspace $\{|+1\rangle_V, |-1\rangle_V\}$ require concatenated pulses.

where one would like to set up entanglement between the vacancy and a nuclear spin in the former's $|m_S = \pm 1\rangle$ subspace and then transfer this bond to a photon via laser excitation of the vacancy, both levels cannot be split by more than the laser pulse's line width of $\approx 100\text{MHz}$ for a short 10ns pulse. Therefore, the magnetic field strength values we settled for are a trade-off between the z-fidelity of the eigenstates on one side and limiting level separation on the other. They are 1.1mT for nearest- and 2mT for third neighbor carbon.

A. Single qubit gates

The pulses and pulse sequences needed for single-qubit control are illustrated in Figure 3. In the following, unless otherwise stated, fidelities and times given apply to a single π -pulse. We also want to distinguish between state-driving fidelity and gate fidelity: the former refers to the fidelity $F_{\rho_0} = F(\mathcal{E}_T[\rho_0], \rho_{\text{target}})$ between the time evolution of one particular starting state and its intended target state, where $\mathcal{E}_T[\rho]$ is the superoperator describing the time evolution of a density matrix ρ until time T and $F(\dots)$ is the fidelity measure as described in Appendix A. Here we usually have $\rho_{\text{target}} = U_{\text{id}}\rho_0 U_{\text{id}}^\dagger$ with U_{id} some desired unitary operation. Gate fidelity is then the minimum of F_{ρ_0} over the entire Hilbert space of our

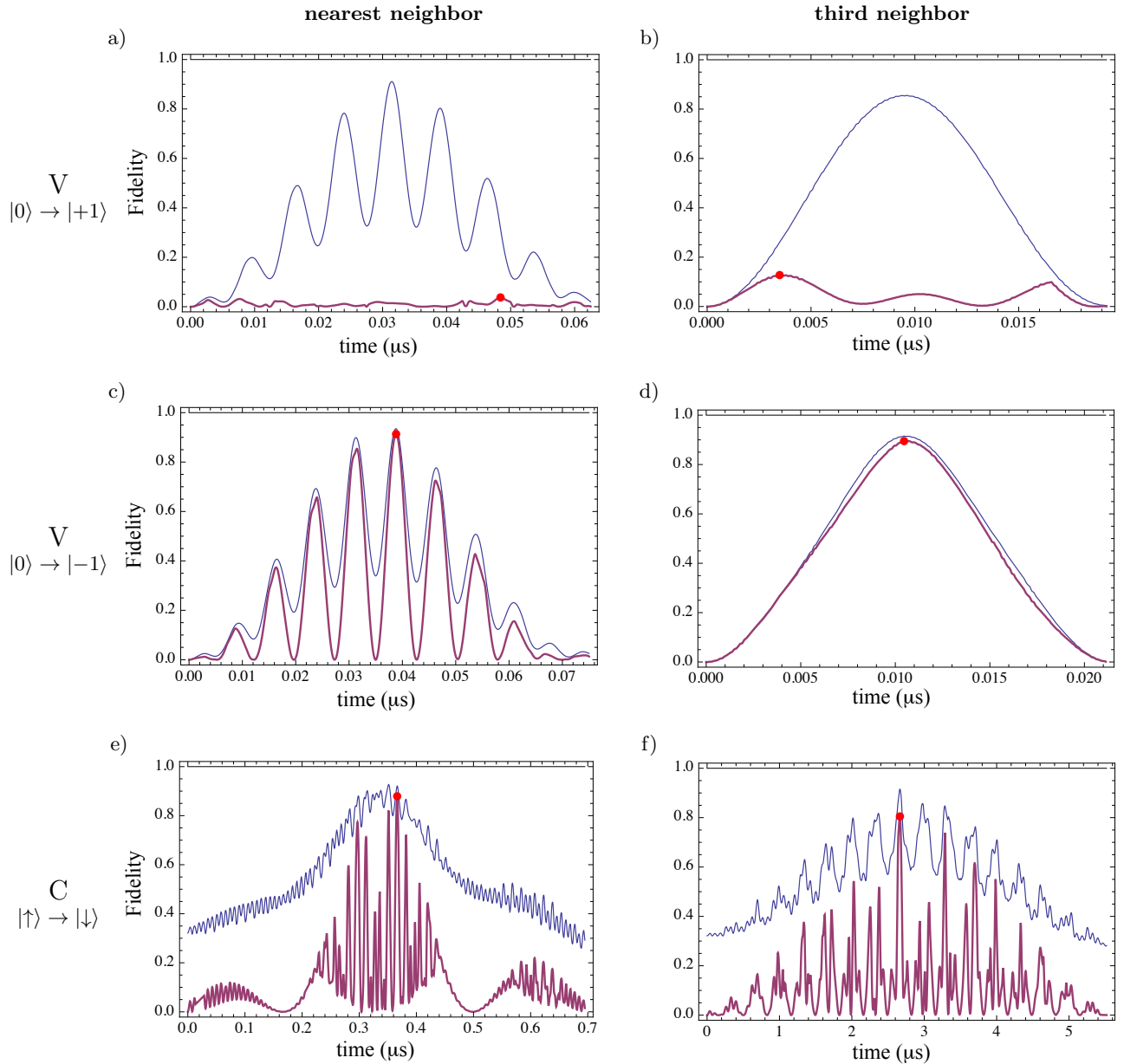


FIG. 4: Low- B π -pulse gate fidelities for the carbon in nearest neighbor (left column) and third neighbor positions (right column). The first column refers to the $|0\rangle_V \rightarrow |+1\rangle_V$ transition the second to $|0\rangle_V \rightarrow |-1\rangle_V$ and the last to $|\uparrow\rangle_C \rightarrow |\downarrow\rangle_C$. The purple trace is the gate fidelity, with the average state fidelity shown in blue as a reference. For the $m_S = +1$ states, individual state pulses are out of phase, resulting in very low gate fidelity, while average state fidelities are similar to the ones for $m_S = -1$.

system: $F(\mathcal{E}, U_{\text{id}}) = \min_{|\psi\rangle \in \mathcal{H}} F_{|\psi\rangle \langle \psi|}$. This is hard to compute exactly even for our modest Hilbert-space dimension of $\dim \mathcal{H}_{\text{NV}+\text{C}} = 12$. Therefore we settled for an approximation by sampling the Hilbert space at representative points. For a detailed description of how we measure fidelity in our numerical implementation we refer to Appendices A and B.

Driving V . — The transition frequency between $|+1\rangle_V$ and $|-1\rangle_V$ is strongly dependent on the state of the carbon nuclear spin for both nearest and 3rd nearest neigh-

bor ^{13}C , which clearly poses a problem for single-qubit operations. We had to solve this in two different ways for the two carbon positions: in the case of nearest neighbor using dual frequency driving ($N_f = 2$ in (4)) works well, while it does not give good results for third neighbors. We attribute this to the much stronger parallel hyperfine interaction in the former case, resulting in a splitting of $\approx C_{\parallel}^{\text{nn}} = 129\text{MHz}$ between carbon $|\uparrow\rangle$ and $|\downarrow\rangle$. This is resolvable within the π -pulse times giving the best fidelities, which are on the order of $\text{O}(10\text{ns})$. In contrast, the splitting is only $\approx 13.5\text{MHz}$ for third nearest neighbor

transition	other	nearest neighbor			third neighbor		
		Ω_0^{opt} (MHz)	fidelity (%)	time T_π (ns)	Ω_0^{opt} (MHz)	fidelity (%)	time T_π (ns)
$ 0\rangle_V \rightarrow +\rangle_V$ $(-1\rangle_V)$	$ \uparrow, \uparrow\rangle_{\text{CN}}$	36 (45)	98.5 (99.0)	19.1 (16.2)	32 (43)	98.3 (99.0)	21.1 (17.2)
	$ \uparrow, x+\rangle_{\text{CN}}$	66 (")	97.1 (97.6)	15.7 (15.9)	48 (")	99.0 (99.1)	14.7 (17.4)
	$ x+, \uparrow\rangle_{\text{CN}}$	50 (")	97.2 (98.0)	16.0 (16.1)	75 (77)	90.0 (91.2)	8.9 (9.9)
	$ x+, x+\rangle_{\text{CN}}$	24 (22.5)	93.2 (94.2)	31.0 (31.1)	74 (76)	89.3 (90.1)	9.0 (9.9)
	$(\frac{1}{2}\sigma_0)_C \otimes (\frac{1}{2}\sigma_0)_N$	" (")	95.3 (95.7)	31.8 (31.5)	" (")	94.1 (94.4)	9.3 (10.5)
	gate avg	22.5(19.0)	4 (91.3)% 90.6 (94.3)%	48.4 (38.8) 32 (38.7)	70 (70) " (")	13.4% (89.2%) 87.1% (91.3%)	3.9 (10.4) 9.8 (")
$ \uparrow\rangle_C \rightarrow \downarrow\rangle_C$	$ +1, \uparrow\rangle_{\text{VN}}$	70	99.2	322	100	99.3	1654
	$ +1, x+\rangle_{\text{VN}}$	61	99.1	335	35	98.5	4649
	$\frac{1}{\sqrt{2}}(+1\rangle + -1\rangle)_V \uparrow\rangle_N$	"	97.4	312	99	95.2	1724
	" $(\frac{1}{2}\sigma_0)_N$	"	98.2	328	"	92.2	1667
	gate avg	51	87.9% 91.8%	367 "	61	80.5% 90.8%	2665 "
$ \uparrow\rangle_N \rightarrow \downarrow\rangle_N$	$ +1, \uparrow\rangle_{\text{VC}}$	100	97.9	16900	135	94.1	6747
	$ +1, x+\rangle_{\text{VC}}$	119	63.6	7025	122	89.6	7043
	$\frac{1}{\sqrt{2}}(+1\rangle + -1\rangle)_V \uparrow\rangle_C$	"	74.2	11600	111	91.4	9134

TABLE I: Maximum fidelities for square pulse driving of various specific starting states as well as gate fidelities for both carbon positions. Gate fidelities refer to the quantity $\max_t \min_j \text{Fid}(\mathcal{E}_t[\rho_{0,j}], \rho_{T,j})$ where \mathcal{E}_t is the time evolution operator and j runs from 1 to the number of initial-target state pairs (25, 16 and 8 for vacancy, carbon and nitrogen).

and therefore not big enough to allow resolution of the two-component pulse within a time of about 10ns. This would rather require one order of magnitude longer pulses *i.e.*, weaker driving power. Unfortunately we found that for such slow pulses maximum fidelity invariably suffers. The best solution in this case is then to apply a fast pulse tuned to the average transition frequency. In principle it holds: the faster the better, but for very short pulse times, timing error will start to seriously reduce the fidelity.

When starting in a polarized state, we find that state fidelities can reach up to 98.5% for nearest neighbor ($|\psi_0\rangle = |-1, \uparrow, \uparrow\rangle_{\text{vcn}}$, $\Omega_0 = 45\text{MHz}$, π -time of $T = 16.2\text{ns}$) and 98.3% for third neighbor carbon ($|\psi_0\rangle = |-1, \uparrow, \uparrow\rangle_{\text{vcn}}$, $\Omega_0 = 30\text{MHz}$, π -time of $T = 25.0\text{ns}$, see Table I). Gate fidelities are significantly lower. In fact, transitions from $m_S = 0$ to $m_S = +1$ show an intriguing disconnect between average and gate fidelity: average fidelity reaches about 90%, similar to $m_S = -1$ transitions. Gate fidelity, as defined above, is however only around 10% or less, showing that the π -pulse times for the individual starting states must be very different ('out of phase'). This is not the case for the transitions between $m_S = 0$ and $m_S = -1$, where the gate fidelity reaches within 2-3% of the average state driving fidelity.

These fidelities are all for single π -pulses. Single qubit gates in the physical basis $\{|+\rangle_V, |-1\rangle_V\}$ require three consecutive pulses and will thus have lower fidelity still. In general, fidelities depend on driving power Ω_0 , but for V this is not as pronounced as for the two nuclear spins.

Driving C. — The level splitting for the carbon is independent of either the state of V or N, thus manipulate the carbon spin state independently. This probably explains why it shows the highest state fidelities of the three subsystems, reaching 99.2% (99.3%) for nearest (third)

neighbors (cp. Table I) if vacancy and nitrogen spins are polarized. Gate fidelity is much lower however, with 88% and 80.5% for nearest and 3rd nearest neighbors respectively.

Driving N. — Similar to the vacancy spin, transition frequencies for the nitrogen nuclear spin depend on the state of the carbon, with a difference between level splittings of $\omega_{N,\uparrow\downarrow} \approx 800\text{kHz}$ between $|\uparrow\rangle_C$ and $|\downarrow\rangle_C$. This means that while the vacancy spin can in principle be in an arbitrary state, C must be polarized to either \uparrow or \downarrow . This is in itself somewhat remarkable, since in our model we have no direct coupling between the nuclear spins. The maximum fidelity is 97.9% for the starting state $|+1, \uparrow\rangle_{\text{VC}}$ while gate fidelity is much lower, mostly due to the energy-splitting difference mentioned as well as drift of the carbon spin phase.

A summary of the results for nearest neighbor and third nearest neighbor carbon is given in Table I.

B. Multi-qubit gates and entanglement

Driven gates. — As we mentioned before, the hyperfine interaction causes transitions for the vacancy and nitrogen to be dependent on the state of the other qubits. While this is a problem when implementing single-qubit gates, it can be used to implement two-qubit gates via driving. Using a qubit basis consisting of $|m_S = 0\rangle$ and either of $|m_S = \pm 1\rangle$ such gates can be implemented with a single pulse. For the basis $\{|+\rangle_V, |-1\rangle_V\}$ there is the difficulty that direct transition between these levels are not dipole-allowed and therefore exceedingly slow when driven directly. Thus, between the $|m_S = \pm 1\rangle$ states, all two-qubit gates involving V must be realized via sequences of at least three entangling pulses plus single-

qubit rotations to tidy up factors of i . Figure 3b shows two examples for such gates.

For example a $\text{CNOT}_{C,V}$ (logical $|0\rangle_C$ corresponds to physical $|\downarrow\rangle_C$) would consist of the sequence $\pi(|+1, \uparrow\rangle_{VC} \leftrightarrow |0, \uparrow\rangle), \pi(|0, \uparrow\rangle \leftrightarrow |-1, \uparrow\rangle), \pi(|0, \uparrow\rangle \leftrightarrow |+1, \uparrow\rangle)$. To be independent of the nitrogen, the pulse times must be fast compared to the nitrogen hyperfine level splitting of 3MHz ($=330\text{ns}$), but slow enough to minimize off-resonant driving of the wrong transition (to $|m_S = -1\rangle$). For $\text{CNOT}_{C,V}$ the two transitions are separated by about 180MHz at $B = 1\text{mT}$ corresponding to roughly 6 ns. Thus, both criteria can only be satisfied to limited degree, with the ideal pulse length being about 45ns per pulse or 135ns in total. A SWAP gate between vacancy and carbon state requires 5 π -pulses (see Figure 3b) and has thus a lower fidelity still.

Entangled states. — As we have seen, implementing multi-qubit gates with high fidelities is difficult in the low magnetic field regime. However, if we aim for something less ambitious, such as preparing some useful state from a known starting state, high fidelities are achievable even when including the nitrogen. As examples, let us look at two entangled states $(|+1, \downarrow\rangle + |-1, \uparrow\rangle)_{VC}/\sqrt{2}$ and $(|+1, \downarrow\rangle + |-1, \uparrow\rangle)_{VN}/\sqrt{2}$. The standard way to reach the former is the three-pulse sequence $\pi/2(|0, \downarrow\rangle_{VC} \leftrightarrow |-1, \downarrow\rangle), \pi(|-1, \downarrow\rangle \leftrightarrow |-1, \uparrow\rangle), \pi(|0, \downarrow\rangle \leftrightarrow |+1, \downarrow\rangle)$ involving only 'allowed' (=single flip) transitions. Similarly, for the latter state we would have $\pi/2(|0, \downarrow\rangle_{VC} \leftrightarrow |-1, \downarrow\rangle), \pi(|-1, \downarrow\rangle \leftrightarrow |-1, \uparrow\rangle), \pi(|0, \downarrow\rangle \leftrightarrow |+1, \downarrow\rangle)$, in both cases assuming a starting state $|0, \downarrow, \downarrow\rangle$. For these sequences we find maximum fidelities of 97.4% (97.3%). However, the presence of the strong hyperfine interaction makes it possible to directly drive ordinarily 'forbidden' transitions involving two simultaneous spin flips. This lets us reach the target states with the two-pulse sequences $\text{MW-}\pi(|0, \downarrow\rangle_{VC} \leftrightarrow |-1, \downarrow\rangle), \text{RF-}\pi/2(|-1, \downarrow\rangle_{VC} \leftrightarrow |+1, \uparrow\rangle)$ and $\text{MW-}\pi(|0, \downarrow\rangle_{VN} \leftrightarrow |+1, \downarrow\rangle), \text{RF-}\pi/2(|+1, \downarrow\rangle_{VN} \leftrightarrow |-1, \uparrow\rangle)$. For these fidelities are 98.5% and 98.9% at optimum gate times of 286ns ($15\mu\text{s}$), significantly better than for the ordinary three pulses. This two pulse scheme works well only for setting up odd-parity Bell states, because the two-spin flip processes are mainly caused by the hyperfine exchange term. Even-parity Bell states would need a counter-rotating term, which is only present for the carbon nuclear spin and there too it is much weaker than the exchange term.

IV. INTERMEDIATE FIELD

For magnetic field strengths between $B \approx 15\text{mT}$ and 50mT the eigenstates are much closer to the S_z - I_z -basis than for low B (see Section II, Fig. 2 b)). If we choose the $|m_S = 0\rangle$ and $|-1\rangle$ levels as our vacancy-qubit basis, we see that while the z-fidelity of some states reaches a maximum only much later, there average peaks in the region around 25mT and this is therefore the value we

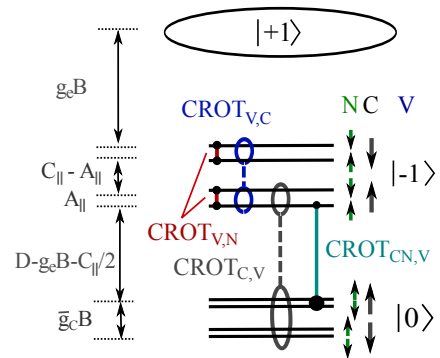


FIG. 5: Energy level schematic with transitions yielding multi-qubit gates. $\text{CROT}_{c[c'], t}$ stands for controlled rotation of qubit t by qubit(s) c (and c'). They are equivalent to a CNOT for one and a TOFFOLI gate for two control qubits

choose. It has the added benefit of large detuning with and thus low leakage into the $|m_S = +1\rangle$ subspace, which has to be avoided as it would constitute a qubit loss error.

A. Single qubit gates

Driving V. — From the energy level structure at intermediate B (Figure 5) one sees, that like in the low-B regime, controlling the vacancy independent of the carbon spin state is again not straightforward. As before, our solution was the dual-frequency driving technique in case of nearest neighbor carbon and driving the average transition frequency in case of third-neighbor carbon. With this, we were able to achieve maximum fidelities of 96.1% and 97.7% respectively. Plots of the gate fidelity for a π -pulse are shown in Figure 6 for both carbon positions. Naturally, state fidelities are higher, up to 99.3% (99.7%) when the nuclear spins are polarized (see Tables II).

Driving C. — Unlike at low magnetic field, fidelities of the carbon nuclear spin nearly match those for the vacancy. Our choice of computational basis means however, we can only effect a π -rotation, if the vacancy spin is polarized into logical $|1\rangle_V$ (the $|m_S = -1\rangle$ state). In our numerical gate fidelity computations we nonetheless included starting states with $|0\rangle_V$, in which case we checked how well the pulse preserves this state, *i.e.*, we set target state equal starting state for the gate fidelity estimation. For nearest neighbor carbon, starting states with the vacancy spin polarized show fidelities up to 99.6% while falling of somewhat if the vacancy starts in the state $|x+\rangle = (|0\rangle_V + |-1\rangle_V)/\sqrt{2}$. There is no significant difference between these starting states in case of third neighbor carbon.

Driving N. — Compared to the low magnetic field regime, nitrogen transition frequencies depend far less on the state of the carbon, which allows relatively good gate fidelities of 96.6% for third nearest neighbor and 94.1%

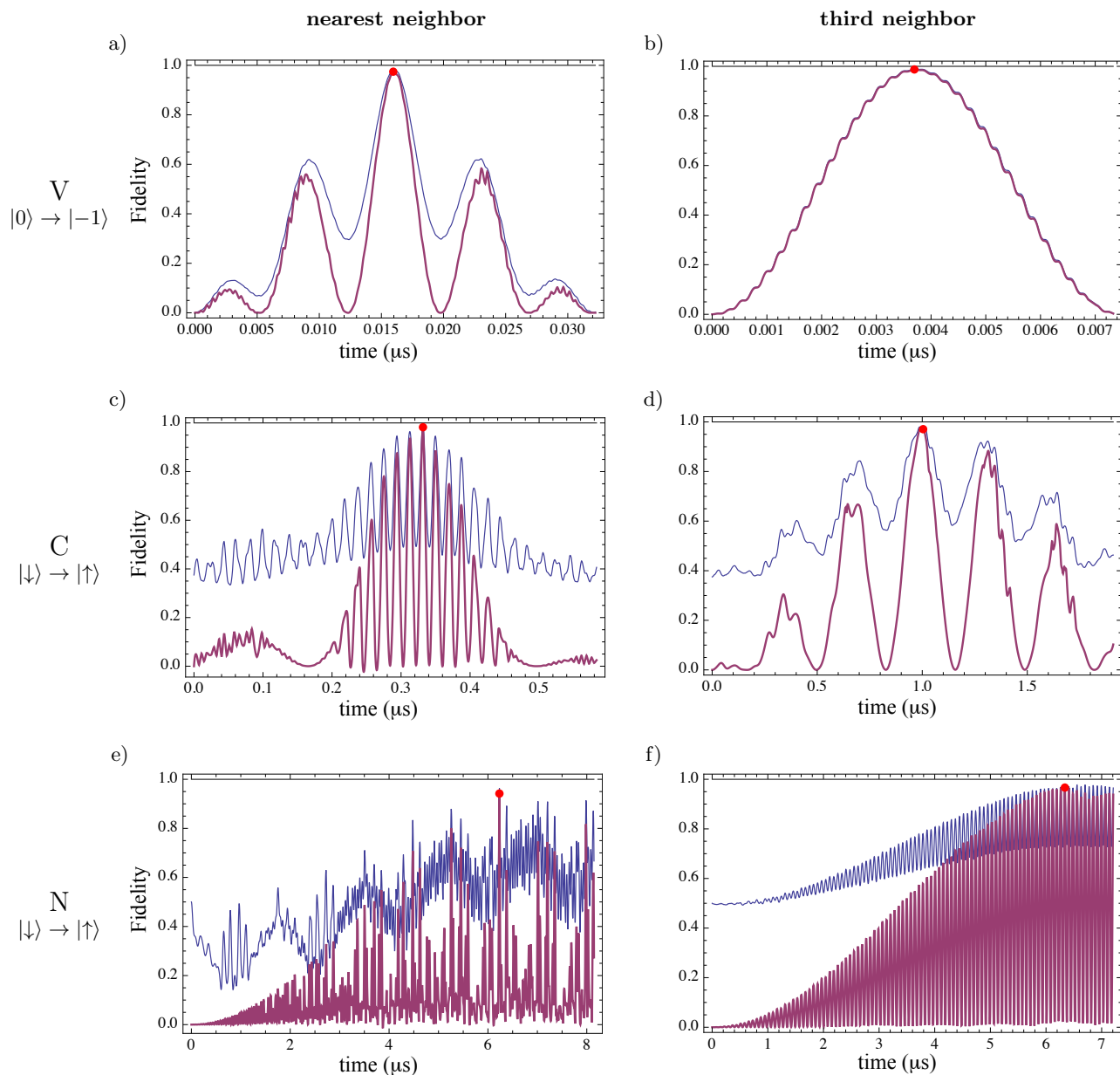


FIG. 6: Gate fidelities of vacancy electron π -pulse driving at low B -field for nearest neighbor (a,c,e) and third nearest neighbor carbon (b,d,f). The horizontal axis shows time in μs and the vertical axis fidelity. Thick, purple traces show the gate, and the thin blue traces average state-driving fidelity. The insets show a zoom-in on each maximum.

for nearest neighbor ^{13}C . With gate times on the order of $6\mu\text{s}$ non-polarized states of the vacancy spin would have dephased strongly due to the low assumed electron T_2 time of $100\mu\text{s}$ (still relatively long for a solid state qubit), which is why excluded them from our gate fidelity computation. Since relaxation is much slower polarized vacancy spin states do not suffer appreciably during the gate time and thus state fidelity for such starting states is as high as for the other subsystems 99.2% and 99.4% respectively for the two different carbon positions.

All results are summarized in Table II for nearest and third neighbor carbons respectively.

Driving power. — Our optimization of the driving power Ω_0 yielded complementary results for nearest and third nearest neighbors. While in the former case, a medium driving power for V and C gates and a quite strong power for N yield the highest maximum gate fidelities, the situation is reversed for 3rd nearest neighbors. That third nearest neighbor V driving should be done fast is understandable because we need linewidths to be larger than the C-spin level splitting of $C_{\parallel} \approx 13.5\text{MHz}$. This is well satisfied for $\Omega_0 \geq 150\text{MHz}$ with sharp peaks in the maximum achievable fidelity occurring whenever the phases can be best lined up. A

A : nearest neighbor

principal	other	Ω_0^{opt} (MHz)	π -pulse fidelity (%)	time T_π (ns)
$ 0\rangle_V \rightarrow -1\rangle_V$ ($\nu = 2125$ MHz)	$ \uparrow, \uparrow\rangle_{CN}$	31	$99.3 \pm .2$	23.4
	$ \uparrow, x+\rangle_{CN}$	44	$98.5 \pm .3$	16.0
	$ x+, \uparrow\rangle_{CN}$	"	98.2 ± 1.3	16.4
	$ x+, x+\rangle_{CN}$	"	98.1 ± 1.2	16.0
	$(\frac{1}{2}\sigma_0)_C \otimes (\frac{1}{2}\sigma_0)_N$	"	$98.7 \pm .3$	16.4
gate:		44	96.1 ± 1.3	16.0
CROT _{C,V}	$\nu = 2123.6$ MHz	43	96.8 ± 0.3	15.8
CROT _{CN,V}	$\nu = 2122$ MHz	0.8	95.2 ± 0.01	932
$ \uparrow\rangle_C \rightarrow \downarrow\rangle_C$ ($\nu = 126.5$ MHz)	$ -1, \uparrow\rangle_{VN}$	31	$99.6 \pm .1$	486.4
	$ -1, x+\rangle_{VN}$	"	$99.6 \pm .1$	486.4
	$\frac{1}{\sqrt{2}}(0\rangle + -1\rangle)_V \uparrow\rangle_N$	32.5	$98.3 \pm .4$	453.1
	" $ x+\rangle_N$	52.5	$98.3 \pm .4$	331.5
	" $(\frac{1}{2}\sigma_0)_N$	"	$98.0 \pm .4$	331.4
gate:		52.7	$98.4 \pm .2$	332
CROT _{V,C}	$\nu = 126.5$ MHz	52.7	97.9 ± 0.1	325
$ \uparrow\rangle_N \rightarrow \downarrow\rangle_N$ ($\nu = 3.13$ MHz)	$ -1, \uparrow\rangle_{VC}$	110	$99.2 \pm .04$	6719
	$ -1, x+\rangle_{VC}$	"	96.2 ± 1.0	7146
	$ -1\rangle_V (\frac{1}{2}\sigma_0)_C$	121	$99.0 \pm .01$	6143
	gate:	109.5	$94.1 \pm .3$	6232
CROT _{V,N}	$\nu = 3.13$ MHz	109	$91.0 \pm .01$	6232

B : third neighbor

principal	other	Ω_0^{opt} (MHz)	π -pulse fidelity (%)	time T_π (ns)
$ 0\rangle_V \rightarrow +1\rangle_V (-1\rangle_V)$ ($\nu = 2181$)	$ \uparrow, \uparrow\rangle_{CN}$	72	$99.7 \pm .2$	9.6
	$ \uparrow\rangle_C \otimes (\frac{1}{2}\sigma_0)_N$	90	$99.4 \pm .2$	7.9
	$ x+, x+\rangle_{CN}$	129	97.2 ± 1.5	3.0
	$ x+\rangle_C \otimes (\frac{1}{2}\sigma_0)_N$	230	97.0 ± 1.6	3.0
	$(\frac{1}{2}\sigma_0)_C \otimes (\frac{1}{2}\sigma_0)_N$	"	97.5 ± 1.6	3.0
gate :		190	$97.7 \pm 0.9\%$	3.7
CROT _{C,V}	$\nu = 2173.4$ MHz	12.5	92.7 ± 0.1	58.0
CROT _{CN,V}	$\nu = 2171.8$ MHz	1.1	97.4 ± 0.01	634
$ \uparrow\rangle_C \rightarrow \downarrow\rangle_C$ ($\nu = 13.45$ MHz)	$ -1, \uparrow\rangle_{VN}$	110	$99.6 \pm .02$	1336
	$ -1, x+\rangle_{VN}$	51	$99.4 \pm .01$	2973
	$\frac{1}{\sqrt{2}}(0\rangle + -1\rangle)_V \uparrow\rangle_N$	72	$99.3 \pm .6$	1980
	" $ x+\rangle_N$	"	$99.2 \pm .11$	1981
	" $(\frac{1}{2}\sigma_0)_N$	72.5	$99.2 \pm .10$	1980
gate:		130.5	$96.9 \pm .02$	1001
CROT _{V,C}	$\nu = 13.5$ MHz	130	98.2 ± 0.05	1082
$ \uparrow\rangle_N \rightarrow \downarrow\rangle_N$ ($\nu = 3.08$ MHz)	$ -1, \uparrow\rangle_{VC}$	83	$99.4 \pm .01$	8847
	$ -1, x+\rangle_{VC}$	101	$98.4 \pm .05$	7649
	$ -1\rangle_V (\frac{1}{2}\sigma_0)_C$	100.5	$98.7 \pm .03$	7563
	gate:	109	$96.6 \pm .01$	6339
CROT _{V,N}	$\nu = 3.13$ MHz	110	98.0 ± 0.02	6553

TABLE II: π -pulse fidelities and times for resonant, square-pulse driving of the NV+C system at $B = 25mT$ for selected states, single- and multi-qubit gates. Gate fidelities were computed from a set of 25, 16 and 8 initial-final state pairs for vacancy, carbon and nitrogen respectively. Uncertainties were computed assuming a timing accuracy of $\Delta t = 250$ ps.

resulting Ω_0 -dependence of the gate fidelity is Figure 7 for the example of a (third neighbor) vacancy electronic spin. While the highest peak in absolute terms occurs at $\Omega_0 \approx 240$ MHz, taking into account the fidelity reduction due to a finite timing accuracy of, assumed, 250ps shows that the first peak at 192 MHz is in fact the preferable choice.

However, in an experimental setup, all optimal driving powers identified in this study are rather technically challenging. Since we consider our system to operate at cryogenic temperatures (~ 4 -8K), sample heating due to

the MW and RF-radiation is a serious issue: a rough estimate for the maximum permissible 'true' driving power is $O(1W)$ for which π -pulse times are roughly 50ns for the vacancy spin. In our model, this gate time occurs for $\Omega_0 = 15$ MHz, which is significantly lower than any of the optimal values we identified (see Table II). This could provide the motivation for an extended search in the low- Ω_0 regime. However the difficulty in such a search would be that computation time is proportional to gate time and thus roughly inversely proportional to Ω_0 . Thus, for all but the vacancy spin, this would make an extensive

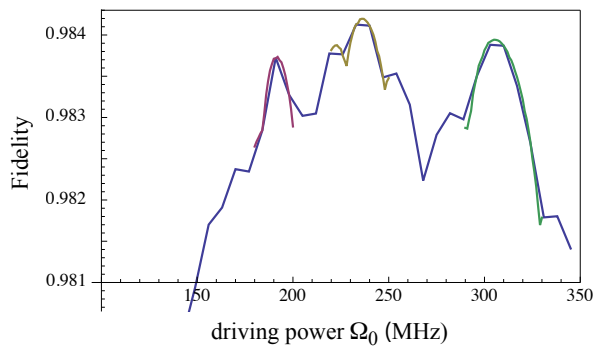


FIG. 7: Ω_0 dependence of the fidelity single-qubit π -pulse fidelity for driving the vacancy nuclear spin in third-nearest neighbor position. The blue trace is from a rough scan (Ω_0 resolution 1MHz), the other curves were computed with finer resolution to reveal the detailed shape of the maxima.

search very difficult.

B. Entangling gates

In the intermediate magnetic field regime, our choice computational basis allows several multi-qubit gates to be implemented by a single pulse. The transitions involved are indicated schematically in Figure 5.

As we see, we can obtain multi-qubit gates between all qubits. This set of operations is redundant in that two CNOTs would already be universal, but this redundancy is very welcome since direct, single-pulse gates are faster and have a higher fidelity than ones obtained from potentially lengthy gate sequences.

The fidelities we find for the gates along with gate times and optimum driving power Ω_0 are given in Table II. Figure 8 shows the fidelity vs. time and the gate matrices at maximum fidelity for two nearest neighbor two-qubit gates.

We should stress, that a gate obtained from 'bare' π -pulse is not directly a CNOT but rather a controlled rotation about the axis determined by the phase angle ϕ of the driving field (see the driving Hamiltonian (4)). E.g. for an ideal π -pulse, the resulting two qubit gate would be $\mathbb{1}_2 \oplus i(\cos(\phi)\sigma_x + \sin(\phi)\sigma_y)$. For $\phi = 0$ this is a CiNOT, necessitating a corrective single-qubit rotation to get an exact CNOT.

In the next section, we will take a closer look at the gates one can derive from this basic set and see what the expected fidelities are.

V. DERIVED GATES AND SEQUENCES

In the previous section we looked at gates and operations implementable with a single pulse. Here we want to extend this to sequences of pulses in order to realize a set of useful gate operations on the three qubit NVC

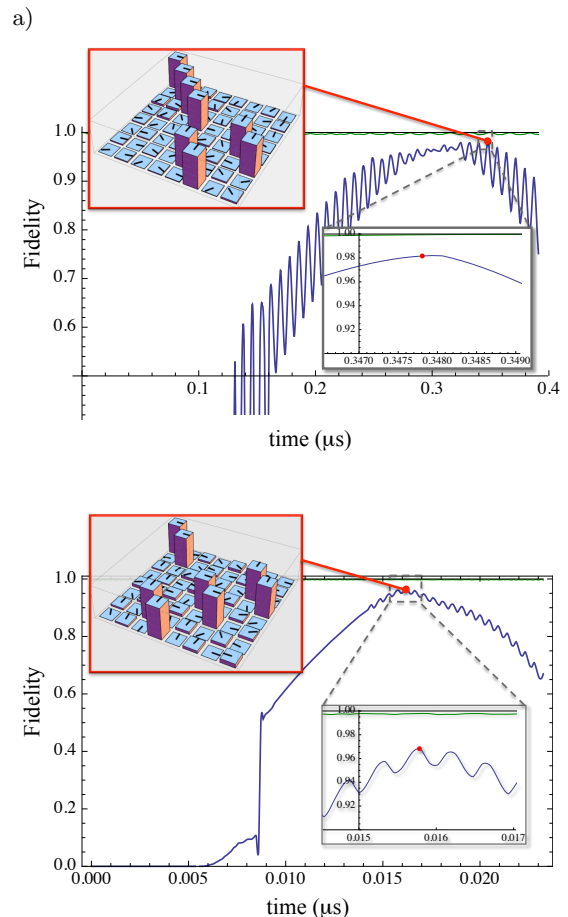


FIG. 8: Two examples of two-qubit gates for nearest neighbor carbon: a) C_VROT_C and b) C_CROT_V . The insets in the upper left visualize the unitary transformation matrices in the computational basis, where the height of a bar stands for the modulus and the small line on top shows the phase. (pointing right = phase 0).

system at intermediate magnetic field. In Figure 9, we show an overview of relevant gates in the NV system both primitive and derived ones together with the dependency structure.

The primitives presented in the previous section include all single-qubit rotations about an axis in the x-y plane (from which one can construct z-rotations), as well as the four entangling operations $CROT_{V,C}$, $CROT_{C,V}$, $CROT_{V,N}$ and $CROT_{C,N,V}$, where $CROT_{1[2],3}$ denotes a conditional rotation applied to qubit 3 controlled by the state of qubit(s) 1 (and 2). For instance, if one chooses to perform an $X(\pi/2)$ rotation, *i.e.*, a π -pulse about the x-axis, the resulting operation would be a CiNOT, which is equivalent to a CNOT up to a $\pi/2$ z-rotation on the control qubit. In addition, one has the non-unitary initialization of the vacancy spin into the $|0\rangle_V$ state. The standard technique at room temperature is to employ off-resonant excitation with green laser light, and was used in virtually all NV experiments to date. However, at low

gate	time (μs)		fid (%)		circuit
	n.n.	3rd nb.	n.n.	3rd nb.	
INIT _V	100		99.9 ^(*)		INIT _V = $ 0\rangle$
MEAS _V	10 μs		"		MEAS _V = $\text{---} $
X, Y _{V/C/N}	.016/.33/6.2	.004/1.0/6.3	96.1/98.4/94.1	97.7/96.9/96.6	$\text{---}[X]\text{---}$, $\text{---}[Y]\text{---}$
CROT _{C,V}	16	4ns	96.8	92.7	CiNOT _{1 2..n} = $\begin{array}{c} 1 \text{---} \bullet \\ \\ 2 \text{---} \bullet \\ \\ \vdots \\ n \text{---} \bullet \\ \\ \text{---}[iX]\text{---} \end{array}$
CROT _{V,C/N}	0.33/6.23	1.08/6.55	97.9/91.0	98.2/98.0	
CROT _{CN,V}	0.93	0.63	94.8	97.4	
Z _{V/C/N}	.032/.66/12.5	.008/2.0/12.7	92/97/89	96/94/93	$\text{---}[Z(\phi)]\text{---} = \text{---}[Y(-\frac{\pi}{2})]\text{---}[X(\phi)]\text{---}[Y(\frac{\pi}{2})]\text{---}$
\mathcal{H} _{V/C/N}	.04/.83/15.6	.01/2.5/15.9	91 / 96/ 86	94/ 92 / 92	$\text{---}[H]\text{---} = \text{---}[Y(\frac{\pi}{2})]\text{---}[Z]\text{---}$
CNOT _{C,V}	.35	1.06	91	94	$\begin{array}{c} 1 \text{---} \bullet \\ \\ 2 \text{---} \oplus \\ \\ \vdots \\ v \text{---} \text{---} \\ \\ n \text{---} \bullet \end{array} = \begin{array}{c} \text{---}[Z(\frac{\pi}{2})]\text{---} \\ \\ \text{---}[iX]\text{---} \\ \\ \text{---}[iX]\text{---} \end{array} = \begin{array}{c} \text{---}[Z(\frac{\pi}{2})]\text{---} \\ \\ \text{---}[iX]\text{---} \\ \\ \text{---}[iX]\text{---} \end{array}$ CPHASE _{CN} = C
CNOT _{V,C}	0.34	1.08	90	94	
CNOT _{V,N}	12.5	12.9	84	94	
CPHASE _{C,N}	1.86	1.26	90	95	
CNOT _{N,V}	43.7	44.6	51	70	
INIT _C	.79	2.24	85	82	INIT _{VX} = $\begin{array}{c} v \text{---} \uparrow \\ \\ x \text{---} 0\rangle \end{array} = \begin{array}{c} 0\rangle \oplus \\ \\ \oplus \end{array}$
INIT _N	56.3	57.6	< 50	66	
SWAP _{VC}	1.03	3.20	79	71	$\begin{array}{c} v \\ \updownarrow \\ x \end{array} = \begin{array}{c} \oplus \oplus \\ \oplus \\ \oplus \oplus \end{array} = \begin{array}{c} \oplus \oplus \\ \oplus \\ \oplus \oplus \end{array}$
SWAP _{VN}	68.7	70.4	< 50	61	
BELL _{VC}	1.5	4.6	84	70	BELL _{VX} = $\begin{array}{c} v \text{---} \oplus \\ \\ x \text{---} \oplus \end{array} \text{---}[H]\text{---} \oplus \oplus$ or $\begin{array}{c} \oplus \oplus \\ \oplus \\ \oplus \oplus \end{array} \text{---}[H]\text{---}$
BELL _{VN}	25.0	25.8	64	83	
BELLM _{VC}	2.75	8.0	67	50	BELLM _{VX} = $\begin{array}{c} v \\ \\ x \end{array} \text{---}[BELL]\text{---} \updownarrow $
BELLM _{VN}	93 .9	96.4	< 50	50	

TABLE III: A list of the relevant gates in the NV+C system with gate times and expected fidelities. Values for primitive gates are taken from the results in Section 4, which in turn are used to estimated those of derived gates. (*) : assumed values

temperature resonant driving to a state with preferential decay to the $m_S = 0$ state, *e.g.* $|A_2\rangle$ is much faster and one should be able to reach high fidelities after only a few cycles.

These primitives clearly form a universal set which has in fact some redundancy. For instance, we need only one out of CROT_{V,C} and CROT_{C,V} as well as CROT_{VN} and CROT_{CN,V}. Having them all at our disposal potentially improves both gate time and fidelity. Table III gives an overview of time and fidelity for the gates shown in Figure 9. It is clear that all gates involving the nitrogen nuclear spin are both slow and low fidelity, so unless this can be resolved by further optimization of square pulses or more advanced pulse shaping, it is best to try and work without it. Excluding the degree of freedom of the nitrogen means we are reduced to a two-qubit system. Thus it is no longer possible to perform any error correction within the device unless we introduce another ^{13}C . However, in such a case we expect similar problems as with the nitrogen. Thus, its use in, *e.g.* repeaters would

depend on the initial entangling link being high-fidelity in the first place. Ways to establish such links probabilistically have been proposed [31, 53] using state dependent reflectivity of cavities together with path-erasure techniques.

If we assume entanglement links between two NVC systems are established with fidelity exceeding 99.9% using this method, a Bell measurement could be performed with fidelity $f_{\text{BELL}} = 70\%$ (74%) (cp. Table III) allowing only a single round of entanglement swapping before link fidelity drops below the classical threshold. This shows that for strongly coupling carbon ^{13}C it is necessary to go beyond the square pulse paradigm and consider shaped pulses and pulse sequences. In technical applications, this would mean a complication that is avoidable in bare NV centers, where square pulses are already good enough. However, we think it is still interesting to pursue this course, as the carbon offers a single-qubit gate speed-up by a factor of more than 10 for nearest- and still about 5 for third-nearest-neighbors.

VI. CONCLUSION

We numerically investigated a system consisting of an $^{15}\text{NV}^-$ center and a nearby, strongly hyperfine-coupled carbon ^{13}C nuclear spin in two different magnetic field regimes. Within a conservative yet realistic model, we determined the achievable fidelities for specific states as well as gates using only simulated square pulses of microwave and radio-frequency radiation. We find that in the low magnetic field regime only some special starting and target state combinations allow high fidelity operations. This suggests that careful selection of states gives us sufficient fidelity to perform some quantum information tasks. Gate fidelity suffers from the limited state z-fidelity and level separation. The situation is much better at intermediate fields. There, we found fidelities of up to 98% for single-qubit gates on the carbon nuclear spin and 97% for the vacancy electronic spin. The nitrogen single-qubit as well as multi-qubit gate fidelities are somewhat

lower than that. If we analyze the expected gate times of gates derived from these primitives via straightforward concatenation, we find that using a strongly bound carbon does indeed offer potential speed up of operations. However the fidelities of these derived gates quickly deteriorates with nesting level. Thus this study indicates that gates implemented via square pulses can be used only in limited applications. For general applications going beyond the square pulse paradigm and using pulse-shaping techniques like optimal control is required.

VII. ACKNOWLEDGEMENT

We thank M.S. Everitt, S.J. Devitt and H. Kosaka for valuable comments and discussions. This research was partially supported under the Commissioned Research of National Institute of Information and Communications Technology (NICT) (A & B) project.

-
- [1] J. Weber, W. Koehl, J. Varley, A. Janotti, B. Buckley, C. Van de Walle, and D. Awschalom, PNAS **107**, 8513 (2010).
 - [2] B. Kane, Nature **393**, 133 (1998).
 - [3] N. Ohlsson, R. K. Mohan, and S. Kröll, Opt. Comm. **201**, 71 (2002).
 - [4] M. W. Doherty, N. B. Manson, P. Delaney, F. Jelezko, J. Wrachtrup, and L. C. Hollenberg, J.Phys.Rep. **528**, 1 (2013).
 - [5] G. Davies, *Properties and growth of diamond* (INSPEC, London, 1994).
 - [6] T. A. Kennedy, J. S. Colton, J. E. Butler, R. C. Linares, and P. J. Doering, Apl. Phys. Lett. **83**, 4190 (2003).
 - [7] F. Jelezko, T. Gaebel, I. Popa, A. Gruber, and J. Wrachtrup, Phys. Rev. Lett. **92**, 076401 (2004).
 - [8] G. Balasubramanian, P. Neumann, D. Twitchen, M. Markham, R. Kolesov, N. Mizuochi, J. Isoya, J. Achard, J. Beck, J. Tisler, et al., Nature Materials **8**, 383 (2009).
 - [9] C. Kurtsiefer, S. Mayer, P. Zarda, and H. Weinfurter, Phys. Rev. Lett. **85**, 290 (2000).
 - [10] R. Brouri, A. Beveratos, J.-P. Poizat, and P. Grangier, Opt.Lett **25**, 1294 (2000).
 - [11] A. Beveratos, R. Brouri, T. Gacoin, J.-P. Poizat, and P. Grangier, Phys. Rev. A **64**, 061802 (2001).
 - [12] F. Dolde, H. Fedder, M. Doherty, T. Nöbauer, F. Rempp, G. Balasubramanian, T. Wolf, F. Reinhard, L. Hollenberg, F. Jelezko, et al., Nature Physics **7**, 459 (2011).
 - [13] C. Degen, Appl. Phys. Lett. **92**, 243111 (2008).
 - [14] G. Balasubramanian, I. Chan, R. Kolesov, M. Al-Hmoud, J. Tisler, C. Shin, C. Kim, A. Wojcik, P. Hemmer, A. Krueger, et al., Nature **455**, 648 (2008).
 - [15] J. Maze, P. Stanwix, J. Hodges, S. Hong, J. Taylor, P. Cappellaro, L. Jiang, M. Gurudev Dutt, E. Togan, A. Zibrov, et al., Nature **455**, 644 (2008).
 - [16] J. Taylor, P. Cappellaro, L. Childress, L. Jiang, D. Budker, P. Hemmer, A. Yacoby, R. Walsworth, and M. Lukin, Nature Physics **4**, 810 (2008).
 - [17] B. J. Maertz, A. P. Wijnheijmer, G. D. Fuchs, M. E. Nowakowski, and D. D. Awschalom, Appl. Phys. Lett. **96**, 092504 (2010).
 - [18] L. T. Hall, C. D. Hill, J. H. Cole, and L. C. L. Hollenberg, Phys. Rev. B **82**, 045208 (2010).
 - [19] A. Cooper, E. Magesan, H. Yum, and P. Cappellaro, Nature Communications **5**, 3141 (2014).
 - [20] J. H. Cole and L. C. L. Hollenberg, Nanotechnology **20**, 495401 (2009).
 - [21] L. T. Hall, J. H. Cole, C. D. Hill, and L. C. L. Hollenberg, Phys. Rev. Lett. **103**, 220802 (2009).
 - [22] L. T. Hall, C. D. Hill, J. H. Cole, B. Städler, F. Caruso, P. Mulvney, J. Wrachtrup, and L. C. Hollenberg, PNAS **107**, 18777 (2010).
 - [23] N. Zhao, J. Honert, B. Schmid, M. Klas, J. Isoya, M. Markham, D. Twitchen, F. Jelezko, R.-B. Liu, H. Fedder, et al., Nat. Nano. **7**, 657 (2012).
 - [24] T. Staudacher, F. Shi, S. Pezzagna, J. Meijer, J. Du, C. Meriles, F. Reinhard, and J. Wrachtrup, Science **339**, 561 (2013).
 - [25] H. Mamin, M. Kim, M. Sherwood, C. Rettner, K. Ohno, D. Awschalom, and D. Rugar, Science **339**, 557 (2013).
 - [26] G. Kucsko, P. Maurer, N. Y. Yao, M. Kubo, H. J. Noh, P. K. Lo, J. Park, and M. D. Lukin, Nature **500**, 54 (2013).
 - [27] W. V. Smith, P. P. Sorokin, I. L. Gelles, and G. J. Lasher, Phys. Rev. **115**, 1546 (1959).
 - [28] J. Loubser and J. van Wyk, Diamond Res. **1**, 11 (1977).
 - [29] F. Jelezko, T. Gaebel, M. Domhan, I. Popa, A. Gruber, and J. Wrachtrup, Phys. Rev. Lett. **93**, 130501 (2004).
 - [30] P. Maurer, G. Kucsko, C. Latta, L. Jiang, N. Yao, S. Bennett, F. Pastawski, D. Hunger, N. Chisholm, M. Markham, et al., Science **336**, 1283 (2012).
 - [31] L. Childress, J. M. Taylor, A. S. Sørensen, and M. D. Lukin, Phys. Rev. A **72**, 052330 (2005).
 - [32] L. Childress, J. M. Taylor, A. S. Sørensen, and M. D. Lukin, Phys. Rev. Lett. **96**, 070504 (2006).
 - [33] N. Yao, L. Jiang, A. Gorshkov, P. Maurer, G. Giedke, J. Cirac, and M. Lukin, Nat. Comm. **3**, 800 (2012).
 - [34] M. V. Gurudev Dutt, L. Childress, L. Jiang, E. Togan,

- J. Maze, F. Jelezko, A. S. Zibrov, P. R. Hemmer, and M. D. Lukin, *Science* **316**, 1312 (2007).
- [35] P. Neumann, J. Beck, M. Steine, F. Rempp, H. Fedder, P. Hemmer, J. Wrachtrup, and F. Jelezko, *Science* **329**, 542544 (2010).
- [36] L. Robledo, L. Childress, H. Bernien, B. Hensen, P. F. Alkemade, and R. Hanson, *Nature* **477**, 574 (2011).
- [37] P. Neumann, N. Mizuochi, F. Rempp, P. Hemmer, H. Watanabe, S. Yamazaki, V. Jacques, T. Gaebel, F. Jelezko, and J. Wrachtrup, *Science* **320**, 1326 (2008).
- [38] E. Togan, Y. Chu, A. S. Trifonov, L. Jiang, J. Maze, L. Childress, M. V. G. Dutt, A. S. Soerensen, P. R. Hemmer, Z. A. S., et al., *Nature* **466**, 730 (2010).
- [39] H. Bernien, B. Hensen, W. Pfaff, G. Koolstra, M. S. Block, L. Robledo, T. H. Taminiau, M. Markham, D. J. Twitchen, L. Childress, et al., *Nature* **497**, 86 (2013).
- [40] P. Neumann, M. Kolesov, B. Naydenov, J. Beck, F. Rempp, M. Steiner, V. Jacques, G. Balasubramanian, M. Markham, D. Twitchen, et al., *Nature Physics* **6**, 249 (2010).
- [41] f. Dolde, I. Jakobi, B. Naydenov, N. Zhao, S. Pezzegna, C. Trautmann, J. Meijer, P. Neumann, F. Jelezko, and J. Wrachtrup, *Nat. Phys.* **9**, 139 (2013).
- [42] T. van der Sar, H. Wang, M. Blok, H. Bernien, T. Taminiau, D. Toyli, D. Lidar, D. Awschalom, R. Hanson, and V. Dobrovitski, *Nature* **484**, 82 (2012).
- [43] T. Taminiau, J. Cramer, T. van der Sar, V. Dobrovitski, and R. Hanson, *Nat. Nano.* **9**, 171 (2014).
- [44] G. Waldherr, Y. Wang, S. Zaiser, M. Jamali, T. Schulte-Herbruggen, H. Abe, T. Oshima, J. Isoya, P. Neumann, and J. Wrachtrup, *Nature* **506**, 204 (2014).
- [45] A. M. Stephens, *Phys. Rev. A* **89**, 022321 (2014).
- [46] M. S. Everitt, S. Devitt, W. J. Munro, and K. Nemoto, preprint (2013), arXiv:1309.3107v1.
- [47] A. Gali, M. Fyta, and E. Kaxiras, *Phys. Rev. B* **77**, 155206 (2008).
- [48] A. Gali, preprint (2009), arXiv:0905.1169v1.
- [49] M. W. Doherty, F. Dolde, H. Fedder, F. Jelezko, J. Wrachtrup, N. B. Manson, and L. C. L. Hollenberg, *Phys. Rev. B* **85**, 205203 (2012).
- [50] S. Felton, A. M. Edmonds, M. E. Newton, P. M. Martineau, D. Fisher, D. J. Twitchen, and J. M. Baker, *Phys. Rev. B* **79**, 075203 (2009).
- [51] R. Hanson, F. M. Mendoza, R. J. Epstein, and D. D. Awschalom, *Phys. Rev. Lett.* **97**, 087601 (2006).
- [52] Z.-H. Wang, G. de Lange, D. Ristè, R. Hanson, and V. V. Dobrovitski, *Phys. Rev. B* **85**, 155204 (2012).
- [53] K. Nemoto, M. Trupke, S. Devitt, A. M. Stephens, K. Buczak, T. Nobauer, M. S. Everitt, J. Schmiedmayer, and W. J. Munro, preprint (2013), arXiv:1309.4277v1.

Appendix A: Measuring fidelity

The fidelity between two quantum states described by density matrices ρ and σ can be determined by

$$F(\rho, \sigma) = \left(\text{Tr} \sqrt{\sqrt{\rho} \sigma \sqrt{\rho}} \right)^2. \quad (\text{A1})$$

The square-root is defined for hermitian operators and can be computed from the eigenspectrum via $\sqrt{\rho} = \text{diag}\{\sqrt{\rho_1}, \dots, \sqrt{\rho_D}\}$ where $D = \dim \mathcal{H}$ and ρ_n are the

eigenvalues of ρ . If one of the states, say σ , is a pure state, this simplifies to

$$F(\rho, \sigma = |\phi\rangle\langle\phi|) = \text{Tr}(\rho |\phi\rangle\langle\phi|) = \langle\phi|\rho|\phi\rangle. \quad (\text{A2})$$

For purely unitary time evolutions, the exact gate fidelity can be computed by just considering (the time evolution of) an ONB of the Hilbert space \mathcal{H} . In practice, this would require computing the time evolution for D different starting states. However, since $\mathcal{E}_t[\rho]$, the actual time evolution of the system, is dissipative in our case, the exhaustive description necessary for calculating the exact gate fidelity requires computing the time evolution for all D^2 generators of the space of hermitian operators on \mathcal{H} . As a standard way of assessing gate-fidelity this is computationally too costly even for our modest Hilbert-space size of $D = 12$.

Therefore, we settled on the practical solution of computing the state fidelities for a suitably large subset of states from \mathcal{H} and taking as our gate fidelity the minimum among all the obtained values. The size of these sets were 25, 16 and 8 states when assessing vacancy, carbon and nitrogen driving pulses respectively. In detail, the state sets were

$$\begin{aligned} \text{Vacancy (25 states): } & \{|0, k, l\rangle, |0\rangle \otimes (\rho_{\text{mixed}})_C \otimes (\rho_{\text{mixed}})_N\} \\ \text{Carbon (16 states): } & \{|m, \downarrow, l\rangle\} \\ \text{Nitrogen (8 states): } & \{|n, l, \downarrow\rangle\}, \end{aligned}$$

where $k \in \{\uparrow, \downarrow, x\pm, y\pm\}$, $l \in \{\uparrow, \downarrow, x\pm\}$, $m \in \{0, -1, x\pm\}$ and $n \in \{0, -1\}$.

Appendix B: Numerical simulation

Decoherence model. — We implemented a master equation in Lindblad form

$$\dot{\rho} = -\frac{i}{\hbar} [H_{\text{VC}}, \rho] + \sum_k \gamma_k \left(L_k \rho L_k^\dagger - \frac{1}{2} \{L_k^\dagger L_k, \rho\} \right). \quad (\text{B1})$$

Here k runs over all subsystems and diagonal/off-diagonal elements, *e.g.* $k = (C, 1+)$ labels the raising operator for the carbon spin, which together with $(C, 1-)$ is responsible for carbon spin relaxation. Thus, the Lindblad operators L_k describe relaxation and dephasing of each system (V, C and N) individually and the γ_k are the inverses of the experimentally observed relaxation and decoherence times T_1 and T_2 of the individual subsystems except for vacancy dephasing rates $\gamma_{2, \text{Va}/b}$. This we chose time dependent, to reproduce the experimentally observed Gaussian (and thus non-Markovian) dephasing of the vacancy electron spin. This kind of dephasing is observed for the time evolution of a spin which evolves under the influence of a weak and randomly varying magnetic field, which in case of the NV stems from other spins in the vicinity (the electronic spins of nitrogen P1 centers as well as carbon ^{13}C nuclear spins). Gaussian

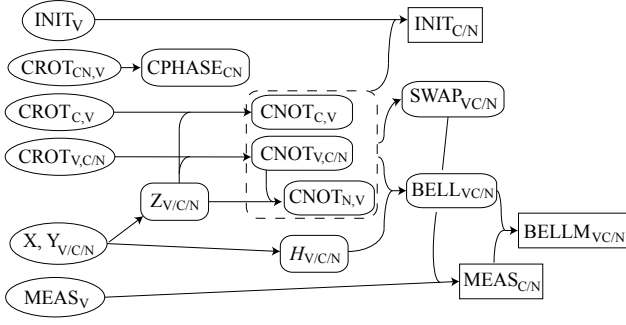


FIG. 9: Graph illustrating the dependencies of derived gates on primitive ones (left side).

dephasing is obtained for a linear time dependence of $\gamma_{2V a/b} = t/T_{2,V}^2$.

Simulation. — Numerical simulations were performed in *Mathematica* (version 7.0) using the built-in `NDSOLVE` function to integrate the Master equation (B1) up to the desired final time starting in some state $\rho(0) = \rho_0$ of the entire system. Single qubit gate fidelities were computed as described in the previous section while multi-qubit gates were extracted in a similar fashion, however comparing each final state to all other target states in addition to the desired one.

Appendix C: Derived gates

In the intermediate field regime ($B = 25\text{mT}$) we computed the fidelities of some interesting derived gates based on the simulation results obtained for primitive gates. Derived gates are constructed from sequences of primitive ones according to some gate identity. Following the prescription of these identities we obtain derived gate parameters by multiplying the fidelities and summing the

times of the constituent primitives. This is consistent with the limitation of the $\text{NV}^- + \text{C}$ system where gates cannot be performed in parallel on different subsystems for physical reasons, even though this might be possible logically (e.g. single-qubit gates on different qubits commute). For dependency between primitives and derived gates, see Figure 9, for the complete list of gates and the (highest fidelity) identities see Table III.

Frequently there are several different ways to obtain a given gate, in particular since our set of primitives is redundant. For instance one can obtain a $\text{CNOT}_{\text{C,N}}$ either by applying the square of a $\text{CNOT}_{\text{CN,V}}$ ($=\text{TOFFOLI}_{\text{CN,V}}$) sandwiched between two Hadamard gates on the nitrogen or, alternatively, via a $\text{CNOT}_{\text{V,N}}$ sandwiched between two SWAP_{VC} . In this case the former is clearly the faster and higher fidelity alternative. However there are also cases where one has to choose between fidelity or speed. For example a BELL_{VC} gate can be achieved either via $\text{CNOT}_{\text{V,C}} \cdot \text{H}_\text{V} \cdot \text{CNOT}_{\text{V,C}}$ or with the same but with V and C switching roles. We must point out that these two options do in fact not give the exact same gate: the former realizes the basis-state mapping $|00\rangle \rightarrow |\psi_+\rangle$, $|01\rangle \rightarrow |\phi_+\rangle$, $|10\rangle \rightarrow |\phi_-\rangle$, $|11\rangle \rightarrow |\psi_-\rangle$ while the latter has instead $|01\rangle \rightarrow |\phi_-\rangle$, $|10\rangle \rightarrow |\phi_+\rangle$, where $|\phi_\pm\rangle$ and $|\psi_\pm\rangle$ denote the even and odd parity Bell states respectively. But both map the computational basis onto a Bell basis, and the permutation between the Bell vectors just requires a slightly different interpretation of measurement results and we can thus regard them as effectively equivalent. But in practice it makes a great difference which one we choose to perform: the former gate identity involves two slow, but higher fidelity CNOTs and one fast Hadamard and vice versa for the latter. Gate times are (for nearest neighbor) 860ns versus 720ns while the fidelities are 84% compared to 74%.